

**NON-CONTACT CHARACTERIZATION OF CARBON NANOTUBE BASED
STRAIN SENSORS USING MILLIMETER WAVES**

by

Seyda Naz Alasahin

A thesis submitted to the Faculty of the University of Delaware in partial fulfillment of the requirements for the degree of Master of Science in Electrical and Computer Engineering

Summer 2022

© 2022 Seyda Naz Alasahin
All Rights Reserved

**NON-CONTACT CHARACTERIZATION OF CARBON NANOTUBE BASED
STRAIN SENSORS USING MILLIMETER WAVES**

by

Seyda Naz Alasahin

Approved: _____
Mark S. Mirotznik, Ph.D.
Co-Professor in charge of thesis on behalf of the Advisory Committee

Approved: _____
Erik T. Thostenson, Ph.D.
Co-Professor in charge of thesis on behalf of the Advisory Committee

Approved: _____
Jamie Phillips, Ph.D.
Chair of the Department of Electrical and Computer Engineering

Approved: _____
Levi T. Thompson, Ph.D.
Dean of the College of Engineering

Approved: _____
Louis F. Rossi, Ph.D.
Vice Provost for Graduate and Professional Education and
Dean of the Graduate College

ACKNOWLEDGMENTS

I would like to thank my advisors Mark S. Mirotznic, Ph.D. and Erik T. Thostenson, Ph.D. for their guidance and encouragement throughout my masters' education. They have always been available for feedback and advisory even during Covid -19 shutdowns. I also thank Amit Chaudhari, Dae Han Sung, and Ellen Gupta for their academic help and support. A special appreciation is extended to my tactful laboratory group for not letting me feel like a foreigner as an only international student among them.

I would also like to express my appreciation to my loving husband. I have always felt his emotional & academic support and comfort during our journey. His help made all the difference. Last but not least, I would like to thank my parents for their encouragement and blessing all the way from Turkey. I could not have done it without them.

Financial support for this research was provided by Ministry of Education in Turkey and National Defense University in Turkey. I would like to express my appreciation to Dogus Ozkan, Ph.D. for his academic support and understanding.

TABLE OF CONTENTS

LIST OF TABLES	vi
LIST OF FIGURES	vii
ABSTRACT	ix
Chapter	
1 INTRODUCTION AND BACKGROUND	1
1.1 Carbon Fibers	1
1.1.1 Graphite	2
1.1.2 Diamond	3
1.1.3 Graphene.....	3
1.1.4 Buckyballs (Fullerenes).....	3
1.1.5 Carbon Nanotubes (CNTs).....	4
1.2 Carbon Nanotubes in Sensing Technologies	6
1.3 Millimeter wave Technology	7
1.3.1 Transmission Through a Waveguide Technique.....	8
1.3.2 Parallel Plate Capacitor Technique	9
1.3.3 Free Space Method	9
1.3.4 Effective Material Properties.....	10
1.3.4.1 Dielectric Materials	11
1.3.4.2 Conductors.....	12
1.3.4.3 Semiconductors	12
1.3.4.4 Plasmas	13
1.3.5 Reflection and Transmission Coefficients of Layered Structures.....	13
2 METHODS AND EXPERIMENTS.....	18
2.1 Sensor Manufacturing	18
2.2 Fabric Tensile Characterization.....	22
2.2.1 Case Study 1- Horizontally Placed Sensors	23
2.2.2 Case Study 2- Vertically Placed Sensors.....	24
2.2.3 Case Study 3- Applied Strains in Wale Direction	24
2.2.4 Repeatability Testing.....	25

2.3	Free Space Millimeter Wave Testing	26
2.4	3-Dimensional Design of Knitted Fabrics	27
3	RESULTS AND DISCUSSION.....	29
3.1	Morphology and the Structure of the CNT-based Strain Sensors	29
3.1.1	Scanning Electron Microscopy Analysis.....	29
3.1.2	3-D Geometrical Modeling.....	30
3.2	Porosity Analysis.....	32
3.3	Case Study – 1 – Horizontally Placed Sensors - Strain Sensitivity.....	33
3.4	Case Study – 2 - Vertically Placed Sensors - Polarization Analysis.....	35
3.5	Case Study – 3- Applied Strains in Wale Direction – Isotropy Analysis	37
3.6	Loading- Unloading Test.....	38
4	CONCLUSIONS AND FUTURE WORK.....	40
	REFERENCES	41
Appendix		
A	DETAILED MEASUREMENTS OF FABRICS BEFORE AND AFTER COATING	45

LIST OF TABLES

Table 2.1	Sizing percentages of each fabric. Fabrics coated with solution 1:1, 1:2, and 1:3.	21
Table 3.1	Measured geometrical parameters under 3 different strains.	31
Table 3.2	Comparison of sensitivities of sensors with 3 different CNT concentrations over 3 different frequencies.	36

LIST OF FIGURES

Figure 1.1	Structure of Graphite. Adapted from Carbon Fiber Composites by Chung, Deborah D.L, 1994 STATE [3].	2
Figure 1.2	Structures of the carbon atom allotropes [13]. a) Graphite b) Diamond c) Fullerene d) Carbon nanotube.	5
Figure 1.3	Schematic diagram of carbon nanotube’s atomic structure. Zigzag and armchair limitations, chiral vector and angle can be seen in red [15].	6
Figure 1.4	Electromagnetic wave spectrum [29].	8
Figure 1.5	An interface separating two medias. Electric fields and dielectric properties are indicated. (Reproduced from [37])	15
Figure 1.6	Single slab representation with indicated dielectric properties for each side. Reproduced from [37].	16
Figure 2.1	Schematic diagram of sensor manufacturing with dip-coating process ..	19
Figure 2.2	Demonstration of metal frame used for tensile testing.....	23
Figure 2.3	(a) Horizontally placed sensor- case study 1, (b) vertically placed sensor configuration-case study 2.	24
Figure 2.4	Setup of case study 3.	25
Figure 2.5	Schematic diagram of the millimeter-wave setup.	27
Figure 2.6	Coordinate points of a single loop of the weft-knitted fabric with marked parameters	28
Figure 3.1	(a) Structure of knitted fabric, (b) individual fibers in a yarn (c) surface of the fiber of the fabric, (d) CNTs on a single fiber of the fabric.....	30
Figure 3.2	AutoCAD design of weft-knitted fabric.	30
Figure 3.3	AutoCAD designs of fabrics with a) no strain b) 20% strain and c) 40% strain.....	31
Figure 3.4	Structure of the Fabric under (a) 0 % (b) 20 % (c) 40 % strain	33

Figure 3.5	(a) Actual and (b) normalized transmission magnitude vs. strain graph for horizontally placed sensors at 85 GHz, 90 GHz and 95GHz.	35
Figure 3.6	Normalized transmission magnitude vs. strain graph for vertically placed 3 sets of sensors at the frequencies 85, 90 and 95GHz.	37
Figure 3.7	Normalized transmission magnitude vs. strain graph for 3 sets of sensors with varying CNT content.	38
Figure 3.8	Normalized transmission magnitude vs time graph with 3 cycles of 4 different discrete applied strains.	39

ABSTRACT

Carbon nanotubes (CNTs) are unique tubular structures with high thermal and electrical conductivity, distinct optical characteristics, and high mechanical stiffness and strength. Carbon nanotube (CNT) composites have widely been used as strain sensors because of their electrical-mechanical coupling behavior. Typically, these piezoresistive sensors require direct measurement of electrical resistance change using an external source connected with wires. This research introduces a new, non-contact measurement method to detect the change in electrical conductivity of carbon nanotube-based strain sensors using high-frequency millimeter wave technology. By analyzing the transmission coefficient from the textile-based CNT composite, we were able to observe the piezoresistive effect. Sensors were characterized over a broad frequency band, from 82 GHz to 100 GHz, with applied strain up to 40%. Fabrics were coated with a sizing composed of an aqueous dispersion of multi-walled CNTs. Sets of fabrics with different CNT concentration were examined to investigate the sensitivity, polarization effects and isotropy properties of manufactured sensors under three different case studies.

Chapter 1

INTRODUCTION AND BACKGROUND

As smart technologies develop, carbon nanotubes (CNTs) have been drawing enormous attention in sensing technologies due to their high aspect ratios, and outstanding electromechanical properties. CNTs can be semiconducting, small gap semiconductors or metallic according to the lattice orientation [1]. This feature allows CNTs to be used in various sensor applications. This chapter gives a detailed review of background information & previous work related to this thesis. It discusses the different types of carbon-based materials, their use as sensors and millimeter wave technology. Millimeter-wave/materials interactions in theory are also explained as a foundation for upcoming chapters.

1.1 Carbon Fibers

While the current type of carbon fibers we use today were first introduced in the 1950's with Union Carbide (Carbonized Rayons), they actually date back to the discovery of light bulbs where they were used as Carbonized Cotton/Bamboo (cellulose) in 1879. Modern use of carbon fibers includes a wide range of industries from aerospace to sporting goods [2] due to their outstanding properties such as high tensile strength, high Young's modulus, good in-plane electrical and thermal conductivity. Carbon fibers can be used in either short or continuous form, and their structure can be crystalline, amorphous, or partly crystalline [3]. Whereas some

allotropes of carbon fibers can exist naturally, some of the most useful ones are man-made.

1.1.1 Graphite

Graphite is a naturally occurring crystal structured carbon allotropes. In practice, carbon and graphite fibers can be used interchangeably. Figure 1.1 shows the molecular structure of graphite. Carbon atoms are linked with high strength covalent bonds and forms a hexagonal layer. The high in-plane modulus of graphite stems from these strong bonds. On the other hand, layers are bonded with weak Van der Waals bonds, which results in a low modulus in that direction [2].

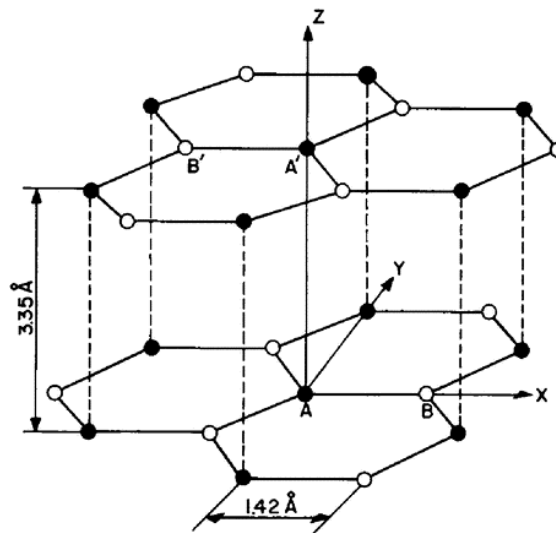


Figure 1.1 Structure of Graphite. Adapted from Carbon Fiber Composites by Chung, Deborah D.L, 1994 STATE [3].

1.1.2 Diamond

As another naturally occurring allotrope of carbon, diamond, has been known for having the highest Young's modulus (~ 1.2 TPa) and its high price. Because it has very strong carbon-carbon covalent bonds (see Figure 1.2b), the melting point of diamond is very high around 4000 °C. It also ranks a 10 on the Mohs Hardness Scale which is used for determining the hardness of solid and minerals [4]. However, because its disadvantages, such as difficulties in processing and high cost, diamond has limited practical applications.

1.1.3 Graphene

Graphene is a single molecular layer of graphite (see Figure 1.2a). In 2004, Andre Geim and Konstantin Novoselov won a Nobel prize for discovery of this man-made carbon allotrope [5]. It has extraordinary properties such as having a high Young's modulus (1 TPa) [6], a breaking strength of 40 N/m and a thermal conductivity of approximately 5000W/mK [7]. Graphene has been used for various applications since its discovery, such as electronics, clothing, conductive inks, and lubrication

1.1.4 Buckyballs (Fullerenes)

Buckminsterfullerenes are the first synthesized allotropes of carbon atom [8]. After their discovery in 1985, the materials industry has entered a new era. Fullerenes are first synthesized by vaporizing solid graphite disks via laser ablation [9] and then arc discharge, carbon vapor deposition (CVD) and joule heating using carbon sources have started being used [10].

1.1.5 Carbon Nanotubes (CNTs)

After advancement of Fullerenes, began the investigation of carbon nanotubes. Carbon nanotubes are tubular structured (see Figure 1.2d), synthesized allotropes of carbon atoms. After their discovery in 1991, they have been used in a large number of practical applications including the reinforcement for a great range of composites. They also have unique and extraordinary electrical and chemical properties. Based on the structure type, carbon nanotubes are classified into two types: single walled carbon nanotubes (SWCNT) and multi-walled carbon nanotubes (MWCNT).

Multi-walled carbon nanotubes are the structures that are composed of more than one SWCNTs. They have a mean Young's Modulus of 1.28 ± 0.5 TPa and they can stand up to 40% strains without a plastic deformation [11]. Similarly, SWCNTs have extremely high elastic modulus that is comparable to diamond. Moreover, their tensile strength is almost 50 times higher than of a high-strength steel with 2 GPa [12]. They also have a high electrical current carrying capability which is estimated to be $1 \times 10^9 \text{ amp} / \text{cm}^2$. That is over 1000 times higher than a copper wire! While the copper wires can only stand up to $1 \times 10^6 \text{ amp} / \text{cm}^2$. While the thermal conductivity of diamond is 3320 W/m K, SWCNTs have a thermal conductivity of 6000 W/mK.

Since above mentioned properties are average (and/or minimum-maximum values), the atomic structure of the nanotubes is one of the cursors for determining the tubes' properties alongside with its morphology. The dimensions (length and diameter). Chiral vector, \vec{C}_h , and chiral angle, θ , are two main factors that describe the atomic structure of nanotubes.

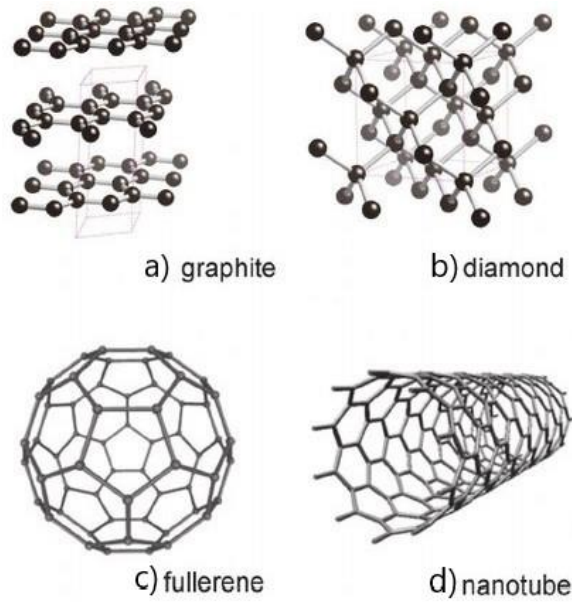


Figure 1.2 Structures of the carbon atom allotropes [13]. a) Graphite b) Diamond c) Fullerene d) Carbon nanotube.

The chiral vector is described by $\vec{C}_h = n\vec{a}_1 + m\vec{a}_2$, where n and m are the number of steps that needs to be taken along the bonds of the lattice, \vec{a}_1 and \vec{a}_2 are unit vectors that can be seen in Figure 1.3. Armchair and Zigzag are two limiting cases where chiral angle is 30° and 0° respectively. It has been stated in [14] that in larger deformations, the elastic properties of carbon nanotubes are found to be sensitive to tube chirality. It is also known that CNTs can be considered as metallic or semi-conducting depending on the chirality [12].

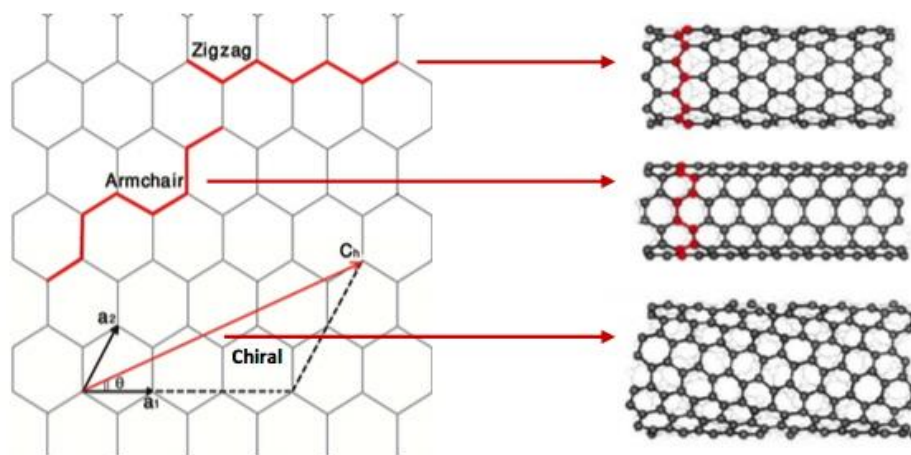


Figure 1.3 Schematic diagram of carbon nanotube's atomic structure. Zigzag and armchair limitations, chiral vector and angle can be seen in red [15].

1.2 Carbon Nanotubes in Sensing Technologies

Strain sensors (gauges) are devices that measure forces on a material under test. They have recently been drawing enormous attention because of their ability to detect, respond and convert mechanical motion into an electrical signal that can be interpreted for several applications. Since their discovery in 1938, they have widely been used in smart bridges, measuring torque, stress, and vibrations of engines. However, some drawbacks such as flexibility issues, ability to only one directional strain measurement, difficulties at low level strain and low sensitivity have started a search for improvements and advancements [16]. CNTs have changed the industry with their capabilities, and began to be widely used as strain sensors.

Many studies focusing on CNTs in aqueous solutions have been conducted throughout years. Rausch et al. [17] investigated the possible interaction mechanisms between the surfactants and the differently functionalized multi-walled CNTs. Bandyopadhyaya et al. [18] studied the stabilization of individual CNTs in aqueous dispersions. Dai et al. [19] stated that it is time consuming to disperse CNTs into the

polymer and introduced a novel two-step method for fabricating CNT-based nonwoven composite strain sensors using a CNT-based aqueous dispersion. They formed an electrically isotropic conductive nanotube network on the surface of the aramid fibers by depositing CNTs. The as-fabricated nanocomposite sensor was mechanically robust, strain sensitive and customizable in shape.

Most studies that focus on CNT based strain sensors used in-contact methods to measure the voltage change in the sensors to determine the sensitivity. While Yasuoka et al. [20], Pham et al. [21], and Park et al. [22] used two-probe method (2 electrodes and a multimeter) to measure the electrical resistivity, Dharap et al. [23,24], Wen et al. [25], Hu et al. [26], and Loh et al. [27] used four-probe measurement method.

1.3 Millimeter wave Technology

Millimeter waves are the electromagnetic waves that have the frequency range of 30 to 300 GHz (see Figure 1.4) which correspond to the wavelengths of 10 mm to 1 mm following the below formula [28].

$$\lambda = \frac{c}{f} \quad (1.1)$$

Where c is the speed of light, $3 \times 10^8 \text{ m/s}$. They fall between microwave and terahertz region with 3 to 30 GHz and 0.1 to 30 THz respectively.

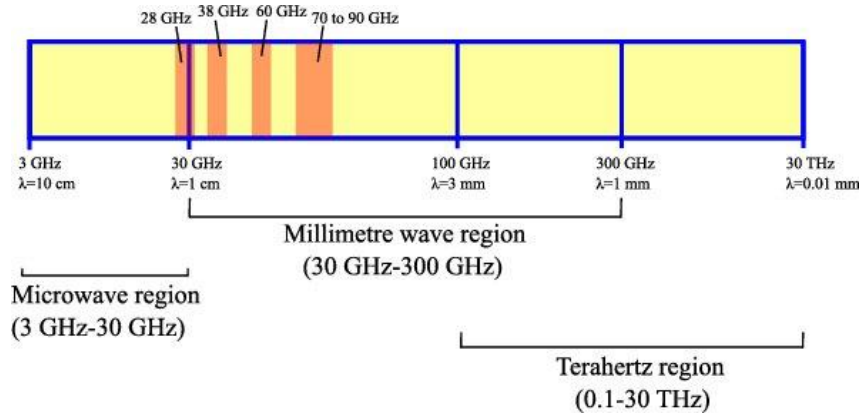


Figure 1.4 Electromagnetic wave spectrum [29].

Millimeter waves have been drawing recent attention for a range of applications in communications and radar. Specifically, these include satellite technologies, radar applications, medical industries, virtual reality setups and 5G communications [30]. Their advantages include but are not limited to large bandwidth, low interference, and small component sizes of setups. However, there are also some drawbacks such as the transmitter and receiver antennas need to have line of sight. Another drawback is the limited range, since millimeter waves have short wavelengths, they could easily be affected by fog, rain or any weather conditions.

One of the many application areas of millimeter waves is the material characterization. There are typically several techniques available such as transmission through a waveguide, parallel plate capacitors or free space methods [31].

1.3.1 Transmission Through a Waveguide Technique

In this technique, sample is put to the contact area of the waveguide, and the parameters S_{11} and S_{12} (reflection & transmission) is measured. It could be

problematic to fit the sample in the waveguide, and any openings between the sample and the waveguide would cause an error in the measurements.

1.3.2 Parallel Plate Capacitor Technique

The parallel plate capacitor technique setup consists of sample in between the parallel plates that are perfect conductors. The sample preparation is easier than most techniques however, an air gap between plates can cause errors as in waveguide technique. The frequencies lower than 1GHz are generally used [32].

1.3.3 Free Space Method

This method is one of the most flexible techniques in terms of its variety in application. It can be used for isotropic- anisotropic materials, different polarizations can be studied, various angles of incidents can be worked on, and a wide variety of frequencies can be used. It consists of 2 horn antennas, and sample in between the antennas. There is little to no sample preparation since there is no-contact between the sample and the setup.

Free space methods have been preferred with waves with high frequencies such as millimeter waves. If the wavelength is smaller than the sample, limitations such as diffraction and charge build up at the edges of sample could be neglected [33]. Since the wavelengths of the millimeter waves are short (10 mm to 1 mm), free space measurements are preferred. These measurements can be conducted with only reflection, only transmission or reflection-transmission models [31]. Reflection-only models can be challenging for some setups as there can be multiple reflections from layers of the material under test. In this study, only transmission coefficients (S_{12}) have been analyzed for estimation of dielectric properties.

In summary, one can estimate the dielectric properties of a material with more than one way. For instance, [34] used transmission line technique (open-ended coaxial dielectric probe and rectangular waveguide techniques) while [35] used parallel plate capacitor and [31] and [36] used free-space method to characterize a material.

1.3.4 Effective Material Properties

In Section 1.3.1 and 1.3.2, the relevant electromagnetic equations follow the derivations found in [37] and [38].

Effective material properties should be mentioned as it is highly related to upcoming sections. A list of quantities and their SI units are given below for convenience.

E: the electric field vector [V/m]

H: the magnetic field vector [A/m]

D: the electric flux density vector [As/m²]

B: the magnetic flux density vector [Vs/m²]

J: the current density vector [A/m²]

The relationship between these quantities in a vacuum are given by

$$D = \epsilon_0 E \tag{1.2}$$

$$B = \mu_0 H$$

where ϵ_0 is the free- space permittivity equal to $\epsilon_0 = \frac{1}{c^2 \mu_0} = 8.854 \times 10^{-12}$ [As/Vm],

and μ_0 is free space permeability with the value $\mu_0 = 4\pi \times 10^{-7}$ [Vs/Am]. C is the speed of light in a vacuum which is equal to 2.99×10^8 [$\frac{m}{s}$]. However, these mentioned

relationships in a material should be defined as:

$$D = \epsilon_0 E + P \tag{1.3}$$

where P is polarization defined as $P = x_e \varepsilon_0 E$, and x_e is the electric susceptibility.

Hence $D = \varepsilon_0 E + x_e \varepsilon_0 E = \varepsilon_0 E(1 + x_e)$. The final equation results in:

$$D = \varepsilon E \quad (1.4)$$

Here $\varepsilon = \varepsilon_r \varepsilon_0$ where ε_r is relative permittivity $\varepsilon_r = 1 + x_e$. The same steps can be applied to magnetic quantities as following

$$B = \mu_0(H + M) = \mu_0(H + x_m H) = \mu_0(1 + x_m)H = \mu H \quad (1.5)$$

Here, $M = x_m H$ is the magnetization and x_m is the magnetic susceptibility.

If we assume the electric field is in the x direction, and a spring like restoring force and a friction-type force exist, a model for estimating dielectric properties of a material can be written as [37]:

$$m\ddot{x} = eE - kx - m\gamma\dot{x} \quad (1.6)$$

where $\dot{x} = dx/dt$, k is the spring constant related to resonance frequency $\omega_0 = \sqrt{k/m}$. So, the equation above can be rewritten as:

$$\ddot{x} + \gamma\dot{x} + \omega_0^2 x = \frac{eE}{m} \quad (1.7)$$

One can divide materials into 4 subcategories as dielectrics, conductors, semi-conductors and plasmas.

1.3.4.1 Dielectric Materials

In dielectric materials, the resonance frequency ω_0 and the rate of collision per unit time γ_0 is different then 0 since there is no force pulling electrons to nuclei, thus no free electron moving around.

$$\omega_0 \neq 0 \ \& \ \gamma_0 \neq 0 \quad (1.8)$$

If we assume electric field is sinusoidal with frequency ω , $E(t) = Ee^{j\omega t}$ then the solution should be $x(t) = xe^{j\omega t}$. When these changes are plugged in to the Equation 1.7 and solved for permittivity, we obtain:

$$\varepsilon(\omega) = \varepsilon_0 + \frac{\varepsilon_0 \omega_p^2}{\omega_0^2 - \omega^2 + j\omega\gamma} \quad (1.9)$$

where $\omega_p^2 = \frac{Ne^2}{\varepsilon_0 m}$ is plasma frequency. Equation 1.9 is known as Lorentz Dielectric.

1.3.4.2 Conductors

As mentioned above, $\omega_0 = 0$ corresponds to free electrons, which means material having the ability to electrically conduct. So, in conductive material case, $\omega_0 = 0$ & $\gamma_0 \neq 0$. When we plug in these conditions, Equation 1.7 becomes:

$$\varepsilon(\omega) = \varepsilon_0 + \frac{\varepsilon_0 \omega_p^2}{-\omega^2 + j\omega\gamma} = \varepsilon_0 + \frac{\sigma(\omega)}{j\omega} \quad (1.10)$$

where $\sigma(\omega)$ is the conductivity that is described by Ohm's law, $J = \sigma \cdot E$, where J is the current density and E is electric field. From that, one could easily conclude:

$$\sigma(\omega) = \frac{j\varepsilon_0 \omega_p^2}{-\omega + j\gamma} \quad (1.11)$$

Equation 1.10 is referred as the Drude Model.

1.3.4.3 Semiconductors

In semiconductors, there are two parts of the equation that needs to be addressed: bound charges and unbound charges. The permittivity can be approximated as:

$$\varepsilon(\omega) = \varepsilon_0 + \frac{\varepsilon_0 \omega_{dp}^2}{\omega_{d0}^2 - \omega^2 + j\omega\gamma_d} + \frac{\varepsilon_0 \omega_p^2}{j\omega(\gamma + j\omega)} \quad (1.12)$$

where ω_{dp} is the oscillator strength of the Lorentz oscillators, γ_d is the spectral width, γ is the damping rate, and ω_{d0} is phonon frequency.

1.3.4.4 Plasmas

The simple model for plasmas can be constructed by assuming $\omega_0 = 0$ & $\gamma_0 = 0$. Therefore, Equation 1.11 becomes:

$$\sigma(\omega) = \frac{\varepsilon_0 \omega_p^2}{j\omega} \quad (1.13)$$

and the corresponding effective permittivity:

$$\varepsilon_0 + \frac{\sigma(\omega)}{j\omega} = \varepsilon_0 + \left(1 - \frac{\omega_p^2}{\omega^2}\right) \quad (1.14)$$

1.3.5 Reflection and Transmission Coefficients of Layered Structures

Let's consider a linearly polarized (in x-direction) electric field and propagating along the z-direction in a lossless dielectric. We would have:

$$E(z) = E_{0+}e^{-jkz} + E_{0-}e^{jkz} = E_+(z) + E_-(z) \quad (1.15)$$

$$H(z) = \frac{1}{\eta} [E_{0+}e^{-jkz} + E_{0-}e^{jkz}] = \frac{1}{\eta} [E_+(z) + E_-(z)] \quad (1.16)$$

where η is the characteristic impedance. By arranging Equation 1.15, we could deduce the following formulas:

$$E_+(z) = E_{0+}e^{-jkz} = \frac{1}{2} [E(z) + \eta H(z)] \quad (1.17)$$

$$E_-(z) = E_{0-}e^{jkz} = \frac{1}{2} [E(z) - \eta H(z)] \quad (1.18)$$

The matrix forms of Equations 1.15 and 1.16 can be expressed as:

$$\begin{bmatrix} E \\ H \end{bmatrix} = \begin{bmatrix} 1 & 1 \\ \eta^{-1} & -\eta^{-1} \end{bmatrix} \begin{bmatrix} E_+ \\ E_- \end{bmatrix}, \quad \begin{bmatrix} E \\ E_- \end{bmatrix} = \frac{1}{2} \begin{bmatrix} 1 & \eta \\ 1 & -\eta \end{bmatrix} \begin{bmatrix} E \\ H \end{bmatrix} \quad (1.19)$$

As a reference for coming sections, wave impedance at z and reflection coefficient at position z is defined below:

$$Z(z) = \frac{E(z)}{H(z)} \text{ wave impedance} \quad (1.20)$$

$$\Gamma(z) = \frac{E_+(z)}{E_-(z)} \text{ reflection coefficient} \quad (1.21)$$

The relationship between wave impedance and reflection coefficient can be expressed as:

$$Z = \frac{E}{H} = \frac{E_+ + E_-}{\frac{1}{\eta}(E_+ + E_-)} = \eta \frac{1 + \frac{E_-}{E_+}}{1 - \frac{E_-}{E_+}} = \eta \frac{1 + \Gamma}{1 - \Gamma} \quad (1.22)$$

$$\Gamma = \frac{E_-}{E_+} = \frac{\frac{1}{2}(E - \eta H)}{\frac{1}{2}(E + \eta H)} = \frac{\frac{E}{H} - \eta}{\frac{E}{H} + \eta} = \frac{Z - \eta}{Z + \eta} \quad (1.23)$$

If we consider a planar interface on xy -plane at some location at z , separating two dielectric/conducting media with characteristic impedances η and η' as shown in Figure 1.5. Since the waves that are linearly polarized in x direction are tangential to the interface that is determined, the boundary conditions should be as below:

$$E = E' \rightarrow E_+ + E_- = E'_+ + E'_- \quad (1.24)$$

$$H = H' \rightarrow \frac{1}{\eta}(E_+ - E_-) = \frac{1}{\eta'}(E'_+ - E'_-) \quad (1.25)$$

From Equation 1.25, we can conclude that the wave impedance is also continuous across interface owing to its definition in Equation 1.20. Equation 1.25 representing electric and magnetic fields can be presented in an arranged matrix form as follows:

$$\begin{bmatrix} E_+ \\ E_- \end{bmatrix} = \frac{1}{\tau} \begin{bmatrix} 1 & \rho \\ \rho & 1 \end{bmatrix} \begin{bmatrix} E'_+ \\ E'_- \end{bmatrix} \quad (\text{matching matrix}) \quad (1.26)$$

and inversely:

$$\begin{bmatrix} E'_+ \\ E'_- \end{bmatrix} = \frac{1}{\tau'} \begin{bmatrix} 1 & \rho' \\ \rho' & 1 \end{bmatrix} \begin{bmatrix} E_+ \\ E_- \end{bmatrix} \quad (\text{matching matrix}) \quad (1.27)$$

where ρ , τ and ρ' , τ' are elementary reflection and transmission coefficients of the left side and the right side of the interface respectively and defined as Equation 1.28.

The matching matrices explains the relationships between forward/backward fields (E_+ and E_- , E'_+ and E'_-).

$$\rho = \frac{\eta' - \eta}{\eta' + \eta}, \quad \tau = \frac{2\eta'}{\eta' + \eta} \quad (1.28)$$

$$\rho' = \frac{\eta - \eta'}{\eta' + \eta}, \quad \tau' = \frac{2\eta}{\eta' + \eta} \quad (1.29)$$

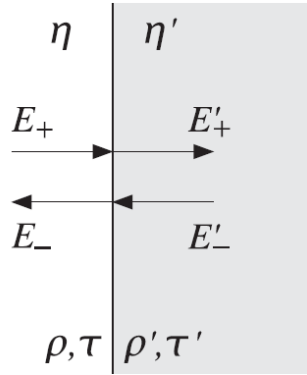


Figure 1.5 An interface separating two medias. Electric fields and dielectric properties are indicated. (Reproduced from [37])

As stated previously, electric field (E), magnetic field (H) and wave impedance (Z) are equal to each other in both side of the interface while backward/forward electric fields (E_{\mp} and E'_{\mp}) are matched with matching matrices derived in Equation

1.26. Now, the relationship between reflection and transmission coefficients on both side of the interface is given in Equation 1.30.

$$\Gamma = \frac{E_-}{E_+} = \frac{\frac{1}{\tau}(\rho E'_+ + E_-)}{\frac{1}{\tau}(\rho E'_- + E_+)} = \frac{\rho + \frac{E'_-}{E'_+}}{1 + \rho \frac{E'_-}{E'_+}} = \frac{\rho + \Gamma'}{1 + \rho \Gamma'} \quad (1.30)$$

$$T = \frac{E'_+}{E_+} = \frac{E'_+}{\frac{1}{\tau}(\rho E'_- + E_+)} = \frac{(1 + \rho)E'_+}{(1 + \rho \frac{E'_-}{E'_+})E'_+} = \frac{1 + \rho}{1 + \rho \Gamma'} \quad (1.31)$$

Similar relationships can be applied to a single slab problem that is illustrated in Figure 1.6. There are 2 different interfaces separating the medias η_a and η_b . The slab has a thickness of l_1 , the propagation wavenumber of k_1 .

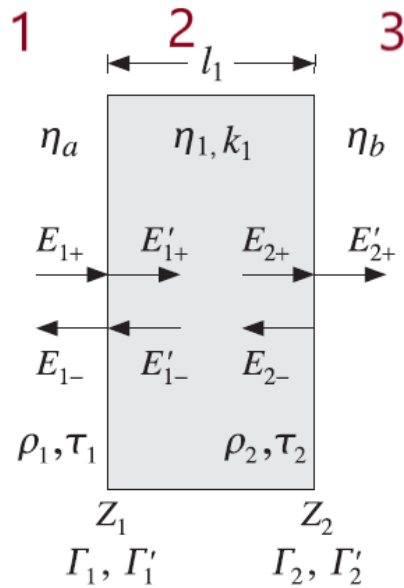


Figure 1.6 Single slab representation with indicated dielectric properties for each side. Reproduced from [37].

To find the elementary reflection and transmission coefficients, we could easily apply the logic of equation 1.28:

$$\rho_1 = \frac{\eta_1 - \eta_a}{\eta_1 + \eta_a}, \quad \tau_1 = 1 + \rho_1 \quad (1.32)$$

$$\rho_2 = \frac{\eta_b - \eta_1}{\eta_b + \eta_1}, \quad \tau_2 = 1 + \rho_2 \quad (1.33)$$

Continuing on equation 1.30:

$$\Gamma = \frac{\rho + \Gamma'}{1 + \rho\Gamma'} \rightarrow \Gamma_1 = \frac{\rho_1 + \Gamma_2 e^{-2jk_1 l_1}}{1 + \rho_1 \Gamma_2 e^{-2jk_1 l_1}} = \frac{\rho_1 + \rho_2 e^{-2jk_1 l_1}}{1 + \rho_1 \rho_2 e^{-2jk_1 l_1}} \quad (1.34)$$

$$T = \frac{E'_+}{E_+} = \frac{1 + \rho}{1 + \rho\Gamma'} \rightarrow T_1 = \frac{\tau_1 \tau_2 e^{-jk_1 l_1}}{1 + \rho_1 \rho_2 e^{-2jk_1 l_1}} \quad (1.35)$$

Where $\Gamma_2 = \rho_2$ since it is assumed that there are no backward-moving waves in medium 3.

This thesis aims to succeed at detecting the conductivity change in strain sensors under strain by using millimeter wave technology. This provides a non-contact measurement method for carbon-nanotube based strain sensor applications.

Chapter 2

METHODS AND EXPERIMENTS

This chapter addresses the methodology used to manufacture carbon nanotube based strain sensors, and testing techniques that was performed to characterize them. The sensors were manufactured with dip-coating method using CNT based aqueous dispersion. Then, three different case studies were performed to investigate the sensitivity and isotropy of the manufactured sensors. The following sections give detailed description of the methodology and thorough experiment preparations.

2.1 Sensor Manufacturing

Sensors were made by depositing carbon nanotubes onto the knitted fabrics using dip-coating method. The solution (SIZICYLTM XC R2G, Nanocyl) that was used to coat fabrics was prepared by mixing an aqueous sizing, where nanotubes and other polymers are randomly dispersed in, with ultra-pure water. A Centrifugal mixer (THINKY® ARM-310) was used to mix the solution at 2000 rpm for 60 seconds to ensure CNTs are uniformly dispersed. The solution then was sonicated for 30 minutes in an ultrasonic bath (Branson® 1510). As a last step, a knitted rectangular fabric (10.16 x 15.24 cm) was selected and dipped into the solution for 20 minutes each side in a flat-bottomed glass container as seen in Figure 2.1. Knitted fabric composed of 44% nylon, 43% polyester, and 13% spandex where spandex provides high stretchability for tensile testing [39]. After this process, CNT coated fabrics were dried in a convection oven at 130°C for 11 minutes.

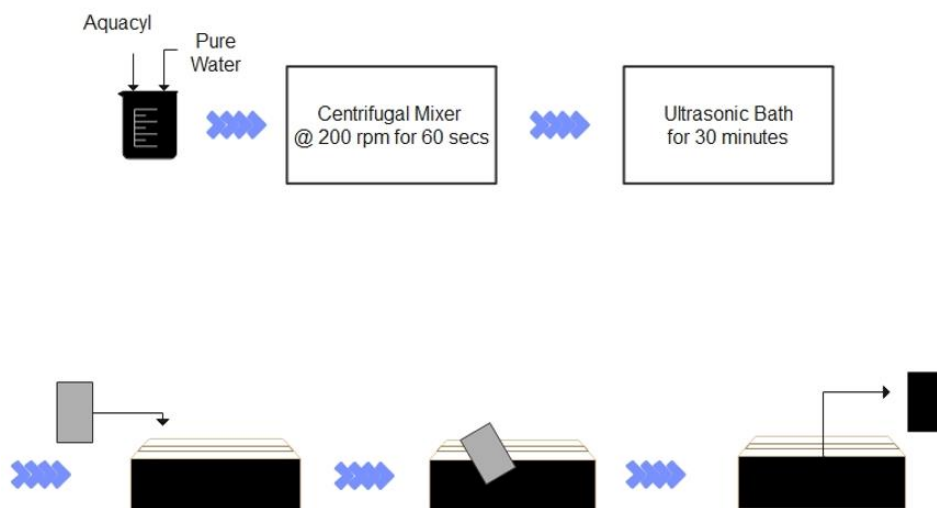


Figure 2.1 Schematic diagram of sensor manufacturing with dip-coating process

A total of three different solutions were made to obtain three different sets of sensors with varying CNT concentrations where each set includes 4 samples to see the consistency of the measurements. Each sensor has the same dimensions of 10.16 x 15.24 cm. Sizing to ultra-pure water mass ratio was 1:1 for the first solution and was 1:2 and 1:3 for the second and third solution, respectively. Aqueous sizing that was used to obtain the coating solution was found to have 3% CNT concentration by weight. Therefore, the overall CNT concentration was 1.5% for the first coating (1:1) solution, 0.1% and 0.75% for the second (1:2) and third (1:3) solution, respectively.

Weights of fabrics were measured before and after coating to calculate CNT concentration of the sensors by weight (CNT weight to fabric weight ratio). Before the initial weighing of the fabrics before coating, they had been heated in the oven at 100°C for 10 minutes to remove any residual moisture. Then, according to the difference of fabric's weights, the CNT concentration by weight on fabrics were calculated in percentages. The average CNT concentration (see Table 2.1) of the first

set of fabrics was 5.47% with a standard deviation of 0.083, and for the second and third sets, these average concentrations were 2.625% and 2.3% with standard deviations of 0.126 and 0.109 respectively.

The fiber volume fractions were calculated according to the formula derived from the rule of mixtures:

$$V_f = \frac{v_f}{v_f + v_m} \quad (2.1)$$

where V_f is the fiber volume fraction, v_f is volume of fibers, $v_f = w_f/\rho_f$, and v_m is the volume of the matrix, $v_m = w_m/\rho_m$. By plugging in the mentioned equations,

$$V_f = \frac{\frac{w_f}{\rho_f}}{\frac{w_f}{\rho_f} + \frac{w_m}{\rho_m}} \quad (2.2)$$

where w_m is weight of fibers and w_m is weight of the matrix. ρ_f and ρ_m represent the density of fibers and matrix, respectively. Using the fiber weight fraction $W_f = w_f/(w_f + w_m)$, the below formula can be obtained.

$$V_f = \frac{\frac{W_f w_m}{\rho_f}}{\frac{W_f w_m}{\rho_f} + \frac{(1 - W_f) w_m}{\rho_m}} \quad (2.3)$$

$$V_f = \frac{W_f}{W_f + \frac{(1 - W_f)\rho_f}{\rho_m}} \quad (2.4)$$

where $\rho_f = 2.26 \text{ g/cm}^3$, $\rho_m = 1.14 \text{ g/cm}^3$.

Table 2.1 Sizing percentages of each fabric. Fabrics coated with solution 1:1, 1:2, and 1:3.

Solution 1:1	Initial weight - Final Weight	Solution Percentages (%)
3	4.304 - 4.553	5.46
4	4.319 - 4.564	5.37
6	4.298 - 4.546	5.45
8	4.327 - 4.583	5.6
Average		5.47+-0.083

Solution 1:2	Initial weight - Final Weight	Solution Percentages (%)
2	4.386 - 4.498	2.49
3	4.406 - 4.527	2.67
4	4.385 - 4.512	2.81
8	4.347 - 4.460	2.53
Average		2.625+-0.126

Solution 1:3	Initial weight - Final Weight	Solution Percentages (%)
3	4.369 - 4.481	2.47
6	4.337 - 4.444	2.31
7	4.336 - 4.434	2.21
8	4.441 - 4.542	2.2
Average		2.3+-0.109

To investigate the solution content stuck on the fabric while sizing, the aqueous solution was weighed before and after each fabric coating. For the solution that has been prepared with 1 portion of water and 1 portion of Nanocyl (1:1), the decrease in the solution during each coating has been observed as 12 grams. Considering it has 1.5% CNT concentration, there are total of 0.18 grams of CNT on each fabric. Thus, the fiber weight fraction $W_{f_{11}} = 0.18 / 4.56 = 3.94\%$. By plugging these parameters in equation 2.4, we obtain the fiber volume fraction of the fabrics that are coated with solution 1:1 as $V_{f_{11}} = 2.02\%$. When the same calculations were done for solutions 1:2 and 1:3, the results are $V_{f_{12}} = 1.36\%$ and $V_{f_{13}} = 0.94\%$ respectively.

A benchtop meter (ACCUMET, AB200 model) with four cell conductivity probe (Fischerbrand Accumet #13-620-165) was used to measure the conductivities of each solution. The solution with the most CNT content, 1:1, was found to have the biggest conductivity with 4.040 mS/cm. Conductivities of solution 1:2 and 1:3 was found to be 2.906 mS/cm and 2.352 mS/cm respectively.

To understand the millimeter-wave testing results better, the change in the fabric structure under strain needs to be investigated. A digital microscope (Dino-lite FC-Z-OZ1) was used to investigate porosity of the manufactured sensors. An LED light source was used to back-light the sensors and the microscope camera captured images of the transmitted light through the sensor. Porosity of the sensors was determined through image analysis. In order to investigate the morphology of the coated CNT-based sensors, scanning electron microscopy (SEM) (AURIGA™ 60 Crossbeam™ FIB-SEM with a 3 kV acceleration voltage) was used.

2.2 Fabric Tensile Characterization

A special metal frame (Figure 2.2) has been designed for tensile testing. There were two grips on each side and one grip in the middle. The sensor was attached between the grip 1 and 2. The grip 2 was moving, which allowed us to stretch the fabrics, thus apply strains. With this device, strains up to 40 % can be applied manually.

Strain levels were calculated by:

$$S(\%) = \frac{\Delta l}{l_E} \times 100 \quad (2.5)$$

where S is the strain in percentage, Δl is the change in the length during stretching, and l_E is the effective length. Effective length is the length between the center of the hollows of grips 1 and 2 on each end of the sensor and is illustrated in Figure 2.2.

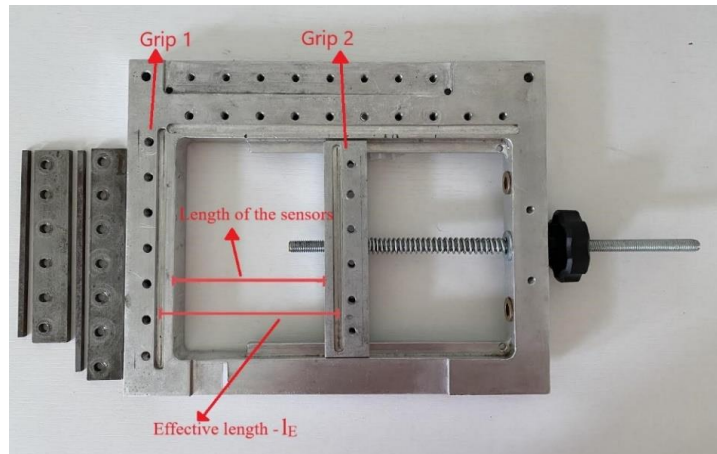


Figure 2.2 Demonstration of metal frame used for tensile testing

2.2.1 Case Study 1- Horizontally Placed Sensors

The structure and the dimensions of the metal frame can be seen in Figure 2.3a. The sensor attached metal frame was mounted to the millimeter-wave testing set up. In this configuration, strain is applied in the opposite direction of antenna polarization, the course direction. The strains from 0% to 40% were applied with 5% separation manually, and the S_{12} parameter was recorded for each strain discretely. Sets of sensors with 3 different CNT concentrations have been tested. Each set consists of 4 identical sensors for consistent and precise results.

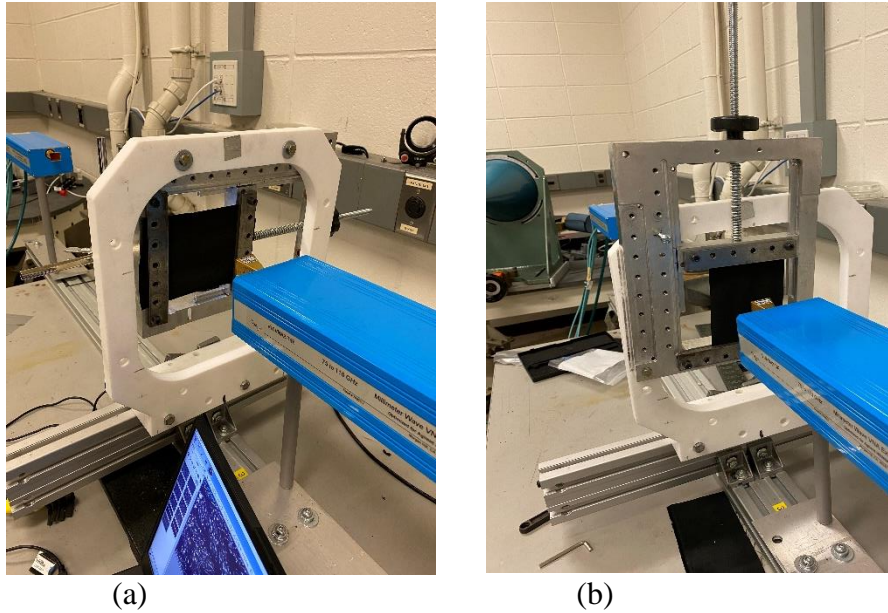


Figure 2.3 (a) Horizontally placed sensor- case study 1, (b) vertically placed sensor configuration-case study 2.

2.2.2 Case Study 2- Vertically Placed Sensors

The sensor frame has been rotated 90°C and attached to the milli-meter wave setup to align the strain direction with the antennas' polarization direction. In this configuration, the direction of strain applied to sensor remained unchanged, however, now, it is applied in the direction of antenna polarization (see Figure 2.3b). The same sequence of strains from up to 40 % applied to the sensors discretely and the parameter S_{12} was observed.

2.2.3 Case Study 3- Applied Strains in Wale Direction

In this case study, isotropy of the sensors was investigated. The sensor frame now is configured as case study 1, so the strain has been applied in the x-direction. However, now the fabric that is attached to it was placed vertically as seen in Figure 2.4. In case study 1 and 2, strain direction respective to the sensor was same and in the

course direction. In this configuration, the applied strain respective to the sensor is in wale direction.

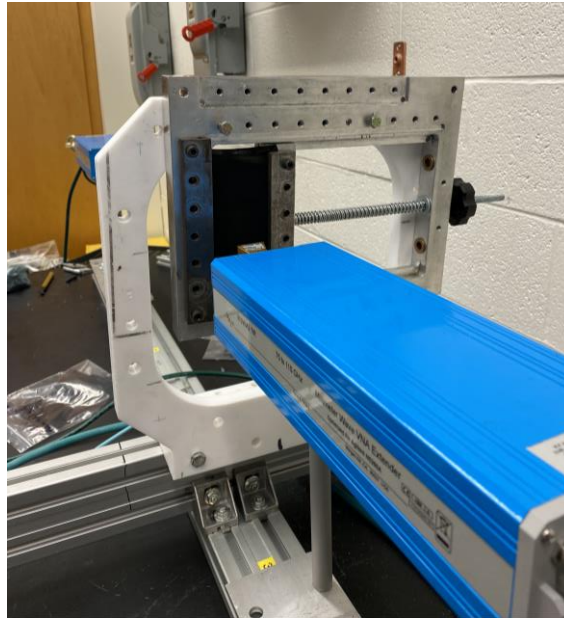


Figure 2.4 Setup of case study 3.

As case study 1 and 2, strains up to 40% with the increments of 5% were applied and S_{12} parameters have been recorded. This configuration has been performed with 3 sets of sensors with different CNT content, each set including 4 identical sensors.

2.2.4 Repeatability Testing

To examine the repeatability of the sensors after applying strains up to 40 %, a loading-unloading test has been performed. The loading-unloading protocol consisted

of 3 cycles of nine strains from 0% to 40% with the increment of 5 %. After each applied strain, the sensor has been brought to resting form (zero strain).

2.3 Free Space Millimeter Wave Testing

Millimeter wave testing setup consists of two vertically polarized antennas with a square Styrofoam frame in the middle to hold the sample frame as seen in Figure 2.5. The two antennas are fully aligned, and the distance between antennas has always maintained constant during the experiments. Due to the small beam width at the sample plane, the metal frame was not directly illuminated and, consequently, did not interfere with the measurement. After a standard thru calibration, the transmission coefficient, S_{21} , was measured from 82 GHz to 100 GHz using an Agilent E8364B Vector Network Analyzer with a N5260A Millimeter Head Controller and high-frequency W-band heads. To remove undesirable reflections, time gating was used with a short time gate window of 0.5 nanoseconds. Transmission data over this band of frequencies was recorded for the range of tensile test conditions described in Section 2.2 for both polarization directions (i.e., case studies 1, 2 and 3).

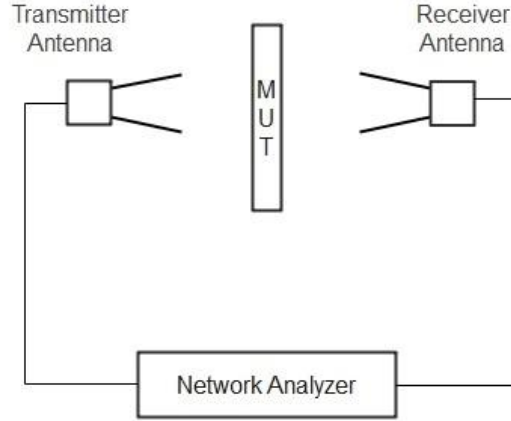


Figure 2.5 Schematic diagram of the millimeter-wave setup.

2.4 3-Dimensional Design of Knitted Fabrics

A 3D solid model of weft-knitted fabrics has been built in COMSOL and AutoCAD under applied tensile strains. This section has been performed to closely observe the structure of the sensors under certain discrete strains. The geometrical modeling that has been described by [40] was performed to simulate the structure of the fabric under strain which includes 9 coordinate points identifying one loop of the weft-knit. The mentioned 9 coordinate points are:

$$\begin{aligned}
 P_1 &= \left(0, 0, \frac{d}{2}\right), P_2 = \left(\frac{c+2d}{4}, \frac{L-w}{2}, 0\right), P_3 = \left(\frac{c}{4}, \frac{L}{2}, -\frac{d}{2}\right), \\
 P_4 &= \left(\frac{c-2d}{4}, \frac{L+w}{2}, 0\right), P_5 = \left(\frac{c}{2}, L, \frac{d}{2}\right), P_6 = \left(\frac{3c+2d}{4}, \frac{L+w}{2}, 0\right), \\
 P_7 &= \left(\frac{3c}{4}, \frac{L}{2}, -\frac{d}{2}\right), P_8 = \left(\frac{3c-2d}{4}, \frac{L-w}{2}, 0\right), P_9 = \left(c, 0, \frac{d}{2}\right)
 \end{aligned}$$

where c is the course length, L is the height of the single loop, w is the wale length and d is the diameter of the yarn represented in Figure 2.6. The parameters c , d , w and L have been determined by image analysis. The parameters were measured for all strains

from 0 to 40% with increments of 5%. Then, according to the 9 coordinate points that was mentioned above, the simulations representing each strain has been designed.

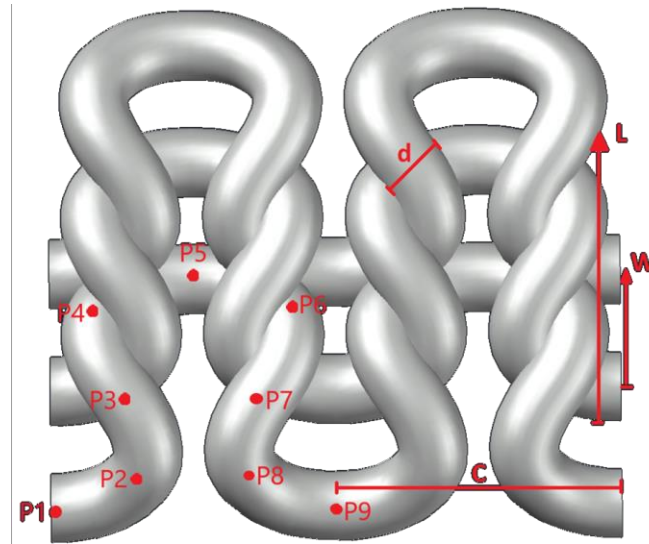


Figure 2.6 Coordinate points of a single loop of the weft-knitted fabric with marked parameters

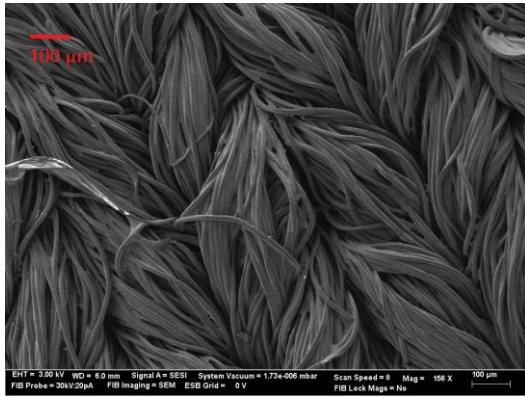
Chapter 3

RESULTS AND DISCUSSION

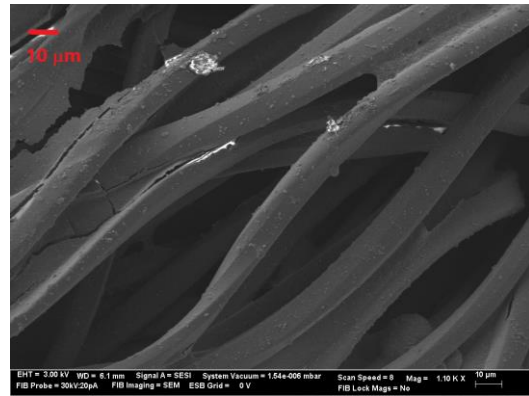
3.1 Morphology and the Structure of the CNT-based Strain Sensors

3.1.1 Scanning Electron Microscopy Analysis

Figure 3.1 shows the morphology of the carbon nanotube-based strain sensors. Figure 3.1a shows the structure of the weft-knitted sensors. As seen in the Figure 3.1a, the yarns are looped horizontally to form a course, and those courses are interlaced to form the wales. Figures 3.1b and 3.1c, with the higher magnification, show the individual fibers in the yarns. In Figure 3.1d, we could see the randomness of the carbon nanotubes in a single fiber due to the nature of dip coating.



(a)



(b)

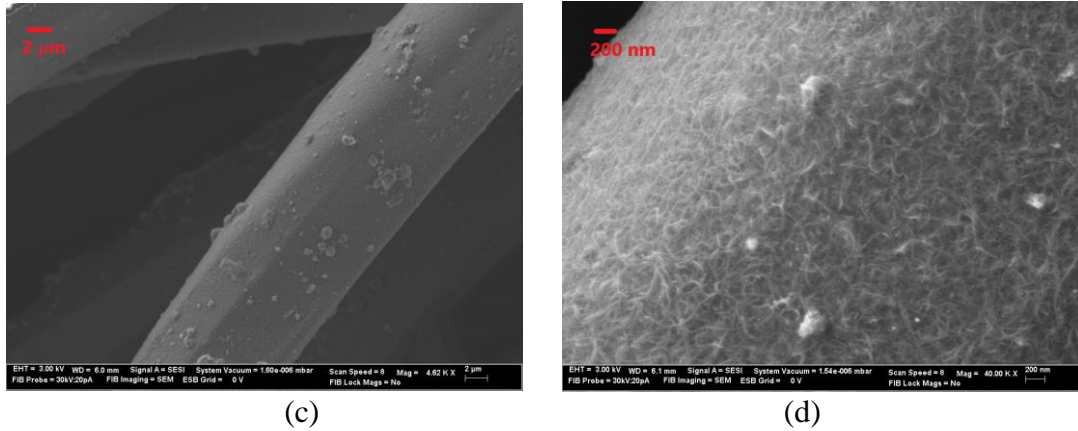


Figure 3.1 (a) Structure of knitted fabric, (b) individual fibers in a yarn (c) surface of the fiber of the fabric, (d) CNTs on a single fiber of the fabric.

3.1.2 3-D Geometrical Modeling

Figure 3.2 shows a solid model of the weft – knitted fabric developed to illustrate how the yarns are interlacing with each other and form the loops. Course and wale directions are indicated.

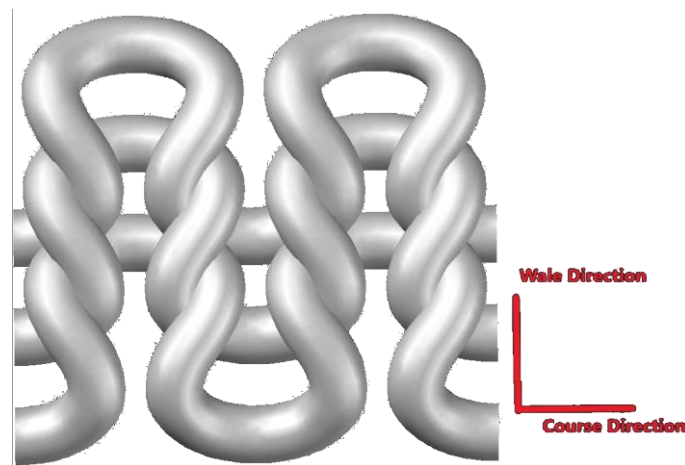


Figure 3.2 AutoCAD design of weft-knitted fabric.

Table 3.1 Measured geometrical parameters under 3 different strains.

Strains \ Parameters	L	W	C	d
0%	0.767	0.425	0.657	0.2
20%	0.664	0.401	0.786	0.2
40%	0.621	0.358	0.904	0.2

The measured geometrical parameters with no strain, 20% and 40% is given in Table 3.1. As the strain is applied in the course direction, we could see the parameter C is increasing with increasing strain while L and W are decreasing. Since there is no significant change in diameter, it is assumed as a constant.

According to the values in Table 3.1, the AutoCAD designs are given in Figure 3.3.:

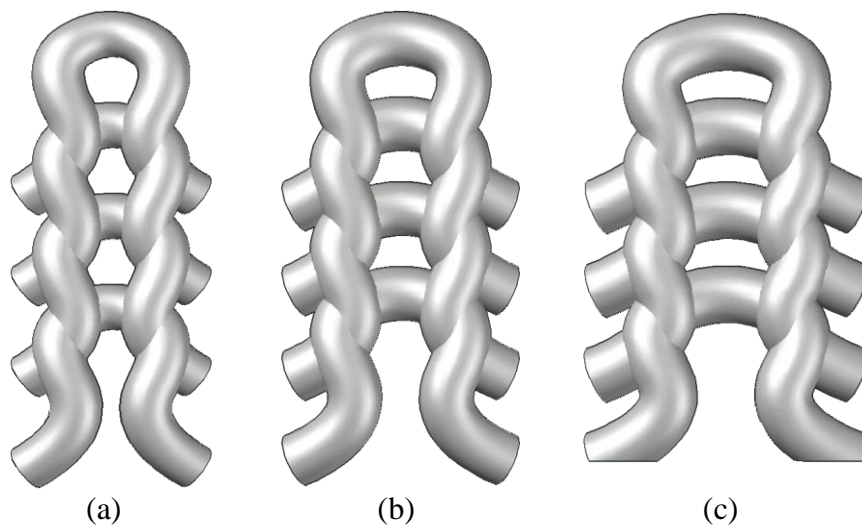
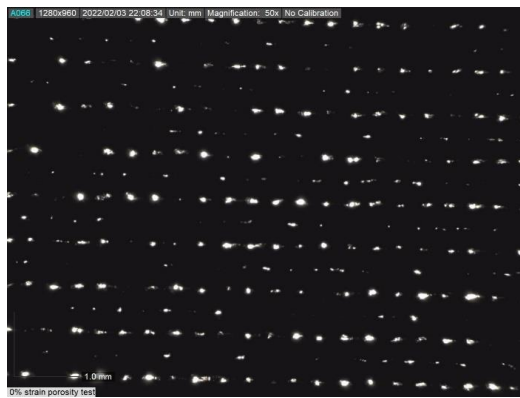


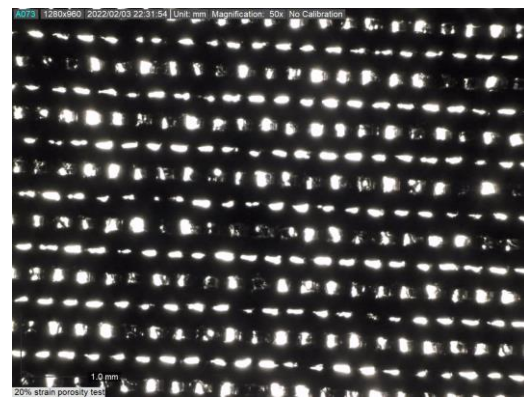
Figure 3.3 AutoCAD designs of fabrics with a) no strain b) 20% strain and c) 40% strain.

3.2 Porosity Analysis

Figure 3.4a shows the fabric structure in resting state, there is no applied strain affecting the fabric. 5.3 x 7.1 mm (the maximum area that can be covered with the used magnification) cell has been drawn on the images. Spherical and rectangular holes have been observed throughout the fabric. Area of each hole has been measured using image analysis, and expressed as the total open area, or porosity. According to these calculations, the porosity of the fabric in resting state has been found as 5.2%. Figure 3.4b shows the fabric structure under 20% strain. The size of the apertures visibly increased thus porosity became 22%. Lastly, for 40% strain (Figure 3.4c), the maximum strain applied to sensors, it increased again to 33%. The void fractions have been found as 5.2%, 8%, 11%, 20%, 22%, 26%, 27%, 29%, 33% for each discrete applied strains from 0% to 40% with the increment of 5%, respectively.



(a)



(b)



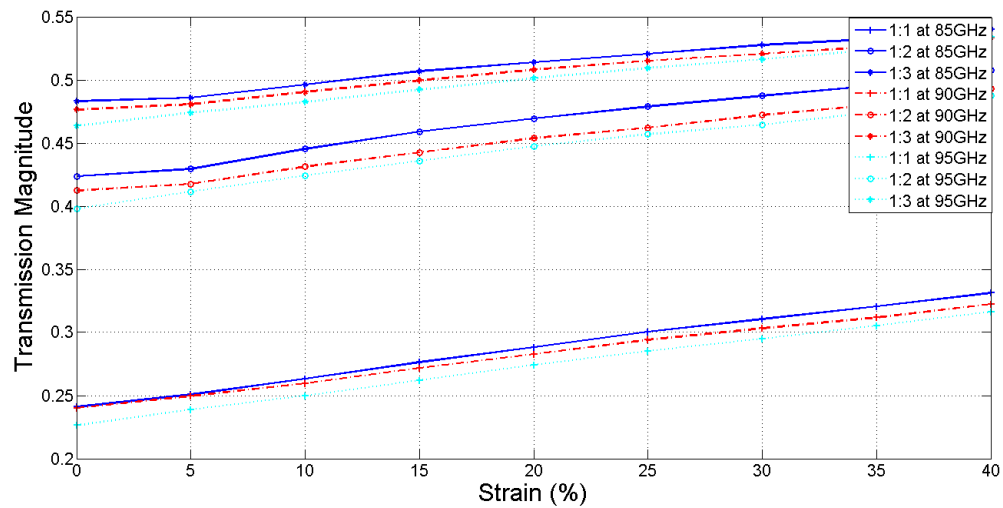
(c)

Figure 3.4 Structure of the Fabric under (a) 0 % (b) 20 % (c) 40 % strain

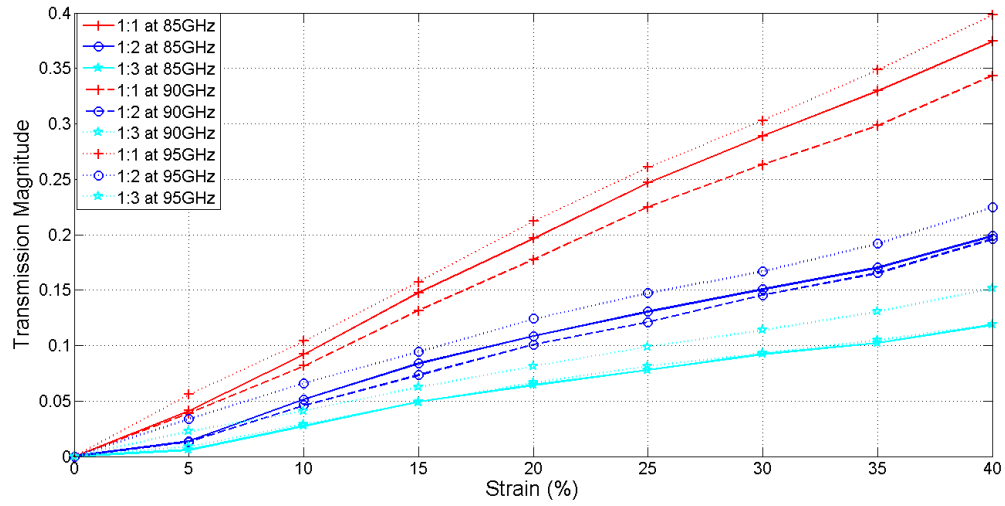
3.3 Case Study – 1 – Horizontally Placed Sensors - Strain Sensitivity

Figure 3.5a shows the actual transmission magnitudes (S_{12}) of the horizontally placed strain sensors at 3 different frequencies. Average of 4 identical sensors have been analyzed for each different sets of sensors with 3 different CNT concentrations. Sensors that are coated with solution 1:1 (highest CNT concentration) have been found to have the lowest transmission magnitude as it is the most conductive one and sensors coated with 1:3 have the highest, as it had the lowest CNT content. As CNT content increases, the sensors get more conductive, and they reflect more signal. Thus, it gives less transmission magnitude. All sensors have showed the same trend. As the strain increases, the transmission magnitude increases, thus sensors are getting less conductive. There is no significant change in the transmission magnitude over the frequency. Figure 3.5b shows the normalized transmission responses of the 3 sets of sensors. They all have been normalized to their initial transmission magnitude at 0% strain. The sensors with higher CNT content found to have the highest sensitivity as they change the most over the strain. This behavior is attributed to the porous structure

of the weft-knitted fabrics. As explained in Section 3.2, the sensors get more porous under increasing strains, and it lets more electromagnetic waves going through the pores of the sensors. When there is higher CNT content, the sensors are getting affected by this porosity more than sensors with lower CNT contents. The slope of the transmission change versus strain graph for sensor that are coated with solution (1:1) has been found as 0.0095 at 85 GHz, 0.0087 at 90 GHz, and 0.0099 at 95 GHz. These slopes for sensor coated with solution (1:2) are 0.005 at 85 and 90 GHz, and 0.054 at 95GHz. Lastly, for sensors with solution (1:3), it is 0.0031 at 85 and 90 GHz, and 0.0037 at 95GHz. Thus, it has been concluded that the sensitivity of sensors coated with dispersion 1:1 was 19 times higher than sensors coated with dispersion 1:2, and 30.6 times higher than the sensors coated with dispersion 1:3.



(a)



(b)

Figure 3.5 (a) Actual and (b) normalized transmission magnitude vs. strain graph for horizontally placed sensors at 85 GHz, 90 GHz and 95GHz.

3.4 Case Study – 2 - Vertically Placed Sensors - Polarization Analysis

Figure 3.6 shows the normalized transmission responses of the vertically polarized sensors at 3 different frequencies 85, 90 and 95 GHz. The same trend as case study -1 applies for all sensors. The sensors have the highest CNT concentration have the lowest transmission magnitude, and the sensors with the lowest CNT content have the highest transmission magnitudes. The sensitivity of the sensors, however, doubled since the strain direction and the polarization direction of the antennas are aligned. While the transmission magnitude changes for horizontally placed sensors were discussed in the last section, the slope values for vertically placed sensors are, for sensors coated with dispersion (1:1), 0.015 at 85 and 90 GHz, and 0.016 at 95 GHz. For sensors with solution (1:2), it is 0.0072 at 85 GHz, 0.0079 at 90 GHz, and 0.0081 at 95 GHz. Lastly, for sensors coated with solution (1:3), the slope of transmission magnitude over strain is 0.0058 at 85GHz, 0.0059 at 90 GHz, and 0.0063 at 95GHz.

To conclude, the sensitivity of the sensors that are coated with solution (1:1), the densest one, has been found to have 2.08 times higher than sensors coated with solution (1:2), and 2.58 times higher than sensors with dispersion (1:3).

Table 3.2 Comparison of sensitivities of sensors with 3 different CNT concentrations over 3 different frequencies.

	Horizontally Placed Sensors	Vertically Placed Sensors	Ratio (V/H)
1:1 at 85 GHz	0.0095	0.015	1.63
1:1 at 90 GHz	0.0087	0.015	
1:1 at 95 GHz	0.0099	0.016	
1:2 at 85 GHz	0.005	0.0072	1.5
1:2 at 90 GHz	0.005	0.0079	
1:2 at 95 GHz	0.0054	0.0081	
1:3 at 85 GHz	0.0031	0.0058	1.824
1:3 at 90 GHz	0.0031	0.0059	
1:3 at 95 GHz	0.0037	0.0063	

For a better comparison, Table 3.2 shows the slope values of sensors with 3 different CNT concentrations, while placed in the setup horizontally, and vertically, respectively. Ratio on the fourth column show the slope values of vertically placed sensors over the slopes of horizontally placed sensors. As it is seen in the table, slopes for horizontally placed sensors changed the most at 85 GHz and there were very insignificant changes for 90 and 95 GHz. On the other hand, for vertically placed sensors (Figure 3.6), slopes did not change significantly at 85 GHz, it increased by 0.0009 at 90 GHz and by 0.0005 at 95 GHz. This yields to the highest ratio of 1.82 with the sensors that are coated with solution (1:3). Sensors with solution (1:1) follow it with the ratio 1.63, and lastly, it is 1.5 for sensors with solution (1:2). Ratios that have been demonstrated in the table were average values of the ratios for the given

solutions. The individual values for the sensors that are coated with solution (1:1) was 1.57 at 85GHz, 1.724 at 90 GHz, 1.616 at 95 GHz. They were 1.44 at 85 GHz, 1.58 at 90 GHz, and 1.5 at 95 GHz for sensors with solution (1:2). Lastly, the values were 1.87 at 85GHz, 1.9 at 90GHz, and 1.7 at 95 GHz.

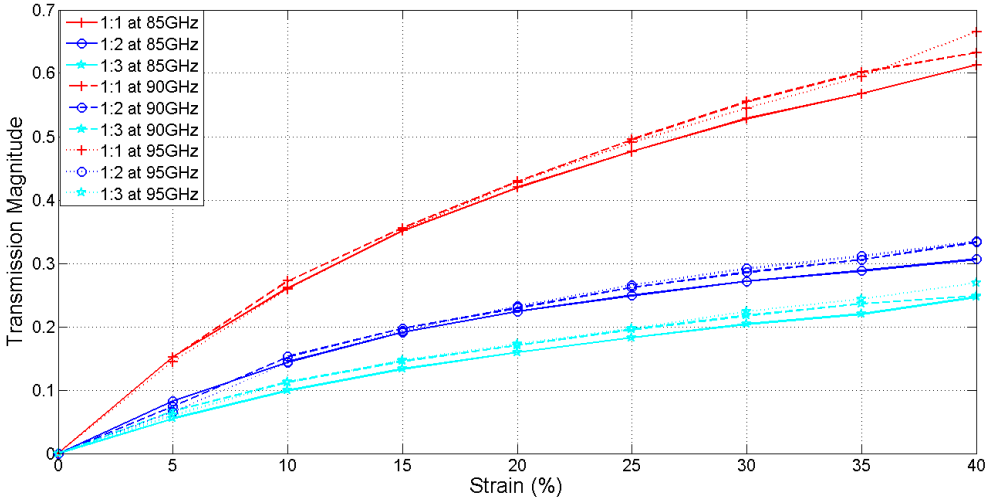


Figure 3.6 Normalized transmission magnitude vs. strain graph for vertically placed 3 sets of sensors at the frequencies 85, 90 and 95GHz.

3.5 Case Study – 3- Applied Strains in Wale Direction – Isotropy Analysis

To investigate the isotropy of manufactured sensors, the frame mounted to the setup horizontally while the sensors were placed vertically. Figure 3.7 shows the normalized transmission magnitude response of the sensors over applied strains up to 40%. Lines in red represent sensors that are coated with solution (1:1), cyan represents sensors coated with solution (1:2), and blue shows the sensors coated with solution (1:3). The same trend as case study 1 and 2 is easily detectable in case study 3. Most conductive sensors in all frequencies have been found to show the most change over

transmission magnitude. This change was the lowest for fabrics coated with solution (1:3). Overall, the transmission response of the manufactured sensors was very similar to the results of case study 1, meaning that whether the strain is applied in wale or course direction, the S_{12} parameters are similar. From this configuration, it can be concluded that the manufactured sensors are isotropic.

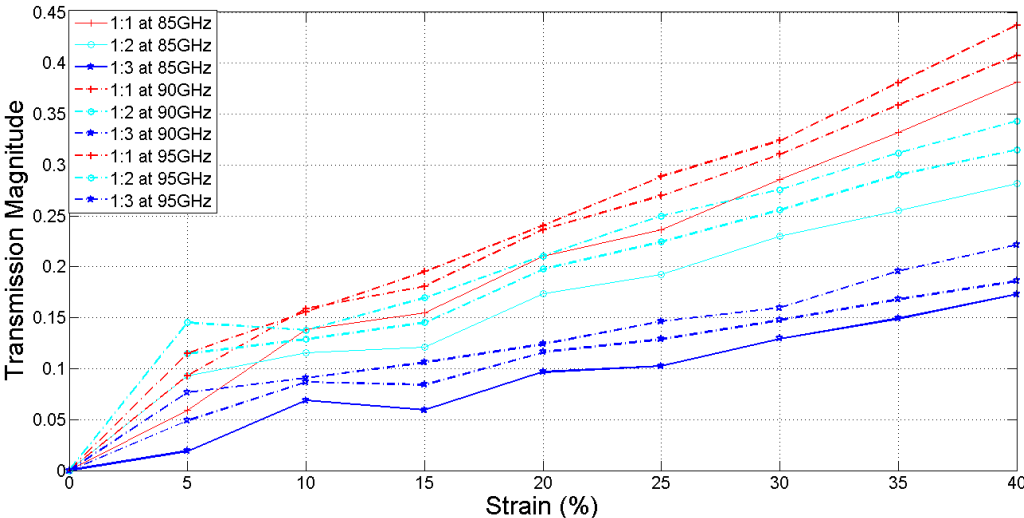


Figure 3.7 Normalized transmission magnitude vs. strain graph for 3 sets of sensors with varying CNT content.

3.6 Loading- Unloading Test

To test the repeatability of the custom manufactured sensors, loading-unloading test that includes 3 cycles of 4 different strains has been performed. The displacement-controlled loading protocol included 4 discrete load-unload cycles: Three to 10 % strain, three to 20 %, three to 30 % and three to 40 % strain. After each strain, the sensor has been set to its resting state (no strain). Figure 3.8 shows the

results of loading-unloading test. The results have been normalized according to the transmission magnitude at 0 %. The sensor response was very consistent, having the same transmission magnitudes at same strains and recovering to the same magnitude every time at 0% except for 2 inconsistencies shown with red circles. Two defects in the figure are attributed to the human error as the strains are applied manually with the help of metal frame. The sensor was not in its complete rest form in 11th and 13th seconds that were marked in Figure 3.8.

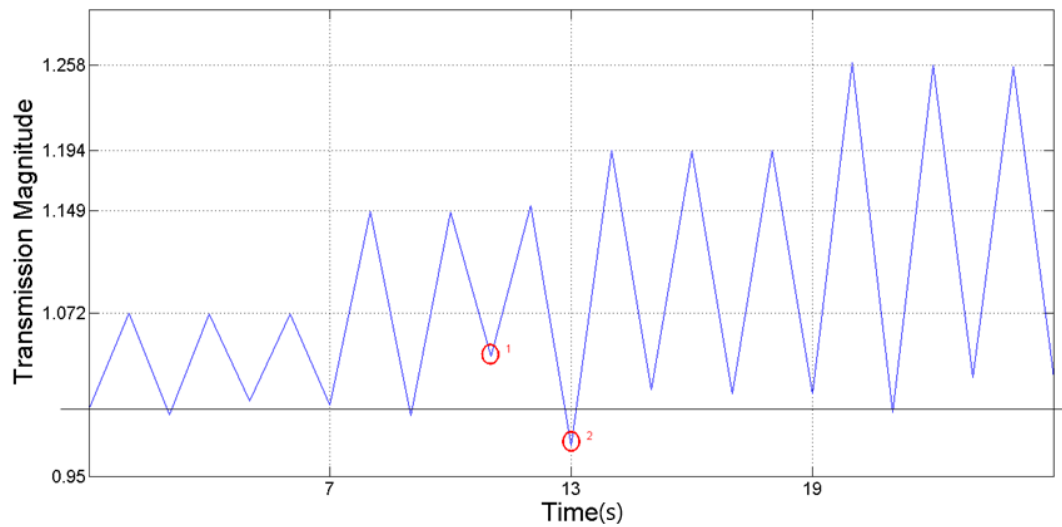


Figure 3.8 Normalized transmission magnitude vs time graph with 3 cycles of 4 different discrete applied strains.

Chapter 4

CONCLUSIONS AND FUTURE WORK

A novel, non-contact measurement method to estimate the change in electrical conductivity of carbon nanotube-based strain sensors using high-frequency millimeter wave technology has been developed. This method was applied over a broad frequency band from 82 GHz to 100 GHz using knitted fabrics that were coated with a sizing composed of an aqueous dispersion of multi-walled CNTs. Samples were tested under varying strain, up to 40%. Two different case studies were conducted to examine the sensor response. The results showed that developed method has been successful to detect the piezoresistive effect where the effective conductivity of the sensor changes with applied strain. Sensors with higher CNT loadings showed higher sensitivities. Sensitivity of sensors with 2.02 % CNT volume fraction has been found to have 30 times higher sensitivity than the sensors with 0.94 % CNT volume fraction. It has been also observed that the polarization affects sensitivities of sensors by a factor of 1.54. When the strain direction and the antenna polarization direction are aligned, sensors showed higher sensitivity responses.

Ongoing research is aimed at developing a computational model predict the millimeter wave properties as a function of strain. This non-contact strain measurement technique has potential for applications ranging from smart technologies to structural health monitoring via enabling remote-control and analysis.

REFERENCES

1. Waris Obitayo, Tao Liu, *A Review: Carbon Nanotube-Based Piezoresistive Strain Sensors*; Journal of Sensors, vol. 2012, 2012.
2. Bhagwan D. Agarwal, Lawrence J. Broutman, K. Chandrashekhara, *Analysis and Performance of Fiber Composites*, 4th edition, Wiley, 2017.
3. Chung, Deborah D.L, *Carbon Fiber Composites*, Elsevier, 1994.
4. Anon, 2021. *Graphite and Diamond - Structure and Properties*. Available at: <https://chem.libretexts.org/@go/page/34175>.
5. Daniel R. Cooper, Benjamin D'Anjou, Nageswara Ghattamaneni, Benjamin Harack, Michael Hilke, Alexandre Horth, Norberto Majlis, Mathieu Massicotte, Leron Vandsburger, Eric Whiteway, and Victor Yu, *Experimental Review of Graphene*; International Scholarly Research Notices, vol. 2012, 2012.
6. Mohammad R. Rahman, M. Moshir Rashid, M. Mashrur Islam and M. Masum Akanda, *Electrical and Chemical Properties of Graphene over Composite Materials: A Technical Review*; Mat. Sci. Res. India, vol. 16, 2019.
7. Dinadayalane, T.C., Leszczynski, J., *Remarkable Diversity of Carbon–Carbon Bonds: Structures and Properties of Fullerenes, Carbon Nanotubes, and Graphene*; Structural Chemistry, vol. 21, 2010, pp. 1155-1169.
8. Hirsch, A, *The Era of Carbon Allotropes*; Nature Mater, vol. 9, 2010, pp. 868-871.
9. R. Bader, W. Lipiński, *Solar Thermal Processing; Advances in Concentrating Solar Thermal Research and Technology*, Woodhead Publishing Series in Energy, 2017, pp. 403-459.
10. Paramita Karfa, Shrabani De, Kartick C. Majhi, Rashmi Madhuri, Prashant K. Sharma, *Functionalization of Carbon Nanostructures*; Comprehensive Nanoscience and Nanotechnology 2nd edition, vol. 2, 2019, pp. 123-144.
11. Waris Obitayo, Tao Liu, *A Review: Carbon Nanotube-Based Piezoresistive Strain Sensors*; Journal of Sensors, vol. 2012, 2012.

12. Erik T. Thostenson, Chunyu Li, Tsu-Wei, Chou, *Nanocomposites in Context*; Composites Science and Technology, vol. 65, 2005, pp. 491-516.
13. Artem R. Oganov, Russell J. Hemley, Robert M. Hazen, Adrian P. Jones, *Structure, Bonding, and Mineralogy of Carbon at Extreme Conditions*; Reviews in Mineralogy and Geochemistry, vol. 75, 2013, pp. 47-77.
14. Guoxin Cao, Xi Chen, *The Effects of Chirality and Boundary Conditions on the Mechanical Properties of Single-walled Carbon Nanotubes*; International Journal of Solids and Structures, vol. 44, 2007, pp. 5447-5465.
15. Moones Rahmandoust, Andreas Öchsner, *Buckling Behaviour and Natural Frequency of Zigzag and Armchair Single-Walled Carbon Nanotubes*; Journal of Nano Research, vol. 16, 2012, pp. 153-160.
16. Abdulkadir Sanli, Abderrahmane Benchirouf, Christian Müller, Olfa Kanoun Chair, *Piezoresistive Performance Characterization of Strain Sensitive Multi-walled Carbon Nanotube-epoxy Nanocomposites*; [Sensors and Actuators A: Physical](#), vol. 254, 2017, pp. 61-68.
17. J. Rausch, R. Zhuang, E. Mäder, *Surfactant Assisted Dispersion of Functionalized Multi-walled Carbon Nanotubes in Aqueous Media*; Composites Part A: Applied Science and Manufacturing, vol. 41, 2010, pp. 1038-1046.
18. R. Bandyopadhyaya, E. Nativ-Roth, O. Regev, R. Yerushalmi-Rozen, *Stabilization of Individual Carbon Nanotubes in Aqueous Solutions*; Nano Letters, vol. 2, 2002, pp. 25-28.
19. H. Dai, E.T. Thostenson, T. Schumacher, *Processing and Characterization of a Novel Distributed Strain Sensor Using Carbon Nanotube-Based Nonwoven Composites*; Sensors, vol. 15, 2015, pp. 17728-17747.
20. T. Yasuoka, Y. Shimamura, A. Todoroki, *Electrical Resistance Change under Strain of CNF/Flexible-epoxy Composite*; Advanced Composite Materials, vol. 19, 2010, pp. 123-138.
21. G.T. Pham, Y.B. Park, Z. Liang, C. Zhang, B. Wang, *Processing and Modeling of Conductive Thermoplastic/Carbon Nanotube Films for Strain Sensing*; Composites Part B: Engineering, vol. 39, 2008, pp. 209-216.

22. M. Park, H. Kim, J.P. Youngblood, *Strain-dependent Electrical Resistance of Multi-walled Carbon Nanotube/Polymer Composite Films*; Nanotechnology, vol. 19, 2008.
23. P. Dharap, Z. Li, S. Nagarajaiah, E.V. Barrera, *Nanotube Film Based on Single-wall Carbon Nanotubes for Strain Sensing*; Nanotechnology, vol. 15, 2004, pp. 379-382.
24. Z. Li, P. Dharap, S. Nagarajaiah, E.V. Barrera, J.D. Kim, *Carbon Nanotube Film Sensors*; Advanced Materials, vol. 16, 2004, pp. 640-643.
25. Sihai Wen and D. D. L. Chung, *Piezoresistivity-Based Strain Sensing in Carbon Fiber-Reinforced Cement*; Materials Journal, vol. 104, 2007, pp. 171-179.
26. N. Hu, Y. Karube, M. Arai, T. Watanabe, C. Yan, Y. Li, Y.L. Liu, H. Fukunaga, *Investigation on Sensitivity of a Polymer/Carbon Nanotube Composite Strain Sensor*; Carbon, vol. 48, 2010, pp. 680-687.
27. K.J. Loh, J.P. Lynch, B.S. Shim, N.A. Kotov, *Tailoring Piezoresistive Sensitivity of Multilayer Carbon Nanotube Composite Strain Sensors*; Journal of Intelligent Material Systems and Structures, vol. 19, 2008, pp. 747-764.
28. David M.SheenDouglas L.McMakinThomas E.Hall, *Chapter 9 - Detection of Explosives by Millimeter-wave Imaging*; Counterterrorist Detection Techniques of Explosives, 2007, pp. 237-277.
29. N. P. Lawrence, B. W. . -H. Ng, H. J. Hansen and D. Abbott, *5G Terrestrial Networks: Mobility and Coverage—Solution in Three Dimensions*; IEEE Access, vol. 5, 2017, pp. 8064-8093.
30. Gayatri Chittimoju and Usha Devi Yalavarthi, *A Comprehensive Review on Millimeter Waves Applications and Antennas*; Journal of Physics: Conference Series, vol. 1804, 2021.
31. O. Buyukozturk , T. Yu, J. A. Ortega, *A Methodology for Determining Complex Permittivity of Construction Materials Based on Transmission-only Coherent, Wide Bandwidth Free-space Measurements*; Cement & Concrete Composites, vol. 28, 2006, pp. 349-359.

32. Jilani. M. T, Rehman. Z, Khan. A. M, Khan. M. T and Ali S. M: *A Brief Review of Measuring Techniques for Characterization of Dielectric Materials*; 2012-13 International Journal of Information Technology and Electrical Engineering, vol. 1, 2012.
33. Leonard Andersson, *Material Characterization by Millimeter-Wave Techniques*; Master Thesis, Department of Electrical and Information Technology, Faculty of Engineering, LTH, Lund University, 2016.
34. W.B. Weir, *Automatic Measurement of Complex Dielectric Constant and Permeability at Microwave Frequencies*; Proceedings of the IEEE, vol. 62, 1974.
35. M. Ken-ichiro, H. Akio, N. Ryusuke, *Broadband Complex Permittivity Measurement Techniques of Materials with Thin Configuration at Microwave frequencies*; Journal of Applied Physics, vol. 98, 2005.
36. D. K. Ghodgaonkar, V. V. Varadan and V. K. Varadan, *Free-space Measurement of Complex Permittivity and Complex Permeability of Magnetic Materials at Microwave Frequencies*; IEEE Transactions on Instrumentation and Measurement, vol. 39, 1990, pp. 387-394.
37. S. J. Orfanidis, *Electromagnetic Waves and Antennas*; Rutgers University, 2016.
38. Sihvola, A. H, and Institution of Electrical Engineers. *Electromagnetic Mixing Formulas and Applications*; IEEE Electromagnetic Waves Series, 47. London: Institution of Electrical Engineers, 1999.
39. Amit Chaudhari, Sagar M. Doshi, Colleen Murray, Erik T. Thostenson, *Highly Sensitive Carbon Nanotube Based Sensors Using Everyday Fabrics for Human Motion Analysis*; SAMPE Conference Proceedings, 2019.
40. Ravandi, Mohammad, Amirreza Moradi, Sean Ahlquist, and Mihaela Banu, *Numerical Simulation of the Mechanical Behavior of a Weft-Knitted Carbon Fiber Composite under Tensile Loading*; Polymers, vol.14, 2022.

Appendix A

DETAILED MEASUREMENTS OF FABRICS BEFORE AND AFTER COATING

1:1 Dipping Count	Initial Weight (grams)	Final Weight (grams)
1	265.38	250
2	250	235.4
3	235.4	215
4	215	202
5	202	190
6	190	177
7	177	165
8	165	154
9	154	142
10	142	130

1:2 Dipping Count	Initial Weight (grams)	Final Weight (grams)
1	180	166
2	166	152
3	152	140
4	140	128
5	128	115
6	115	100
7	100	89
8	89	77
9	77	66
10	66	55

1:3 Dipping Count	Initial Weight (grams)	Final Weight (grams)
1	277	266
2	266	255
3	255	243
4	243	233.5
5	233.5	222
6	222	210
7	210	198
8	198	188
9	188	177
10	177	165